Simulations of a compressible two-layer mixed-flows model with a semi-implicit fractionnal step algorithm on staggered meshes

Olivier Hurisse

Simulations of a compressible two-layer mixed-flows model with a semi-implicit fractionnal step algorithm on staggered meshes

O. Hurisse

1 Introduction

In many industrial processes, fluids are transported in pipes or ducts: for food industries, in drinking-water network, in the processes of the chemical industries ... When focusing on nuclear power plants, in particular for Pressurized Water Reactors (PWR), many examples may be exhibited because all the main processes involve water. Several loops are indeed used in which pressurized water flows thanks to pumps. For instance in the primary circuit of PWR, the circulation of the water around the nuclear core is ensured by a closed loop over the vessel. This loop uses pipes in which the mass flow rate is imposed by a pump. In some classical accidental scenario it is considered that some gas or vapor may be mixed with the water flowing in the loop. Such flows could then lead to a poor functioning of the pump or a blockage of the flow rate. The simulation of these situations is then of prime interest for safety studies in the nuclear industry.

The starting point of the present work is the model proposed in [8, 9, 10]. The latter has shown its capability to treat mixed flows of air and water in pipes with gravity effect. Very complex configurations such as a pipe with a siphon have been tested with very satisfactory results. The two main assumptions made in order to build the model are: the fluid flows in a pipe with a constant section and the flows are stratified, namely the gas phase layer is always over the liquid phase layer. The resulting compressible two-layer mixed-flow model (nicknamed CTL model in the following) is a two-fluid model which can be seen as an extension of the isentropic Baer-Nunziato model (i.e. the Baer-Nunziato model without energy equations). The reader can refer to [1] for the original Baer-Nunziato model (among many other references) and to [26] for a study of the properties of the isentropic Baer-Nunziato model. Moreover, an analogy has been exhibited in [6] between the isentropic Baer-Nunziato model and a two-layer model in pipes. The two-layer model proposed in [3] is different from the CTL model introduced in [8, 9, 10]. In particular, the latter is unconditionally hyperbolic which ensures a time stability of the solution for the initial value problems associated with the model.

The CTL model is thus based on a mass balance equation and a momentum balance equation for each phase, supplemented by an equation describing the space-time evolution of the height of the liquid phase or the gas phase in the pipe. Two major differences with the isentropic Baer-Nunziato model arise. First, convective terms in non-conservative form allow to account for some of the interfacial effects. In the CTL model, they are modified in order to include the gravity effect. Then, due to these modifications, additional terms have to be added to the source terms in order to ensure that they comply with the minimization of the energy of the system. As a consequence, the relaxation source terms that are obtained are slightly changed with respect to the isentropic Baer-Nunziato model. The source terms proposed in [8, 9, 10] are highly non-linear with respect to the primitive variable (i.e. the heights, the partial masses and the momentums). In the present work, the latter have been modified following [20]. The main advantage of these new source terms is that they are more linear with respect to the primitive variables enabling to build schemes that solve convective terms and source terms in a coupled manner.

The simulation of two-fluid models is very often performed using fractional step approaches in which convection terms and source terms are treated separately, see for instance [27, 17, 16, 23, 24, 28, 25] among many other references. One known drawback of these numerical techniques is that the underlying operator splitting implies a decoupling of the different physical effects. In some situations where these different effects strongly interact, this may lead to poor results on coarse meshes which are a target for industrial applications. In [8, 9, 10] efficient numerical schemes have been tested, mainly on the basis of fractional step approaches and using colocated finite volumes schemes. Some numerical schemes for the Baer-Nunziato model have also been tested in [7] by using staggered schemes and they seem promising. It is worth mentioning that when dealing with multi-dimensional complex geometries with unstructured meshes, the definition of staggered schemes has to be performed carefully, as proposed for instance in [11, 12, 19, 18]. In the sequel, the CTL model is only defined for a one-dimensional domain which is a simpler configuration. It is thus quite straightforward to extend the classical SIMPLE projection method [4, 2, 5, 21, 22] to the CTL model for staggered meshes

using a MAC scheme [14, 13, 15]. Thanks to the new form of the source terms proposed here, coupling the source terms to the convective terms in the different steps of the SIMPLE algorithm can be done in a natural way.

The manuscript is organized as follows. The mathematical properties of the CTL model are not recalled here, many details can already be found in [8, 9, 10]. Nevertheless the set of equations for the CTL model is recalled in section 2. Then the description of the numerical strategy is given in section 3: the algorithm for the time stepping (SIMPLE method) is described in section 3.1 and the scheme used to approximate the spacial derivatives (MAC scheme) is detailed in section 3.2. In section 4, a verification test case is proposed and it allows to grasp the behavior and performance of the numerical scheme, while the relaxation effects due to the source terms are investigated in section 5 on a basic test case representative of the flows in the primary circuit of a PWR.

2 The compressible two-layer mixed-flow model (CTL)

In the following, the whole model is presented. The two subsections are devoted to different physical effects. We first present the convective part of the model in section 2.1. This part of the model involves first-order derivative in time and space. They include coupling terms between the two phases. The remaining of these coupling terms appear in the form of source terms that define interfacial exchanges between the phases. The latter are presented in section 2.2.

First of all, an EOS has to be provided for each phase. We choose a complete EOS in the form of the internal energy as a function of the specific volume and the specific entropy: $(\tau_k, s_k) \mapsto e_k(\tau_k, s_k)$. All the thermodynamical quantities can be defined though the phasic Gibbs relation:

$$d_k e_k = T_k d_k s_k - P_k d_k \tau_k,$$

where $d_k.$ stands for the derivative along a streamline of phase k, and where T_k and P_k are respectively the temperature and the pressure of phase k. We assume now that each phase evolves following an isentropic path, that is: $s_k = S_k^0$ with S_k^0 constant an uniform. The phasic Gibbs relation above then simplifies in:

$$d_k e_k = -P_k d_k \tau_k.$$

By abuse of notation, the argument (τ_k, S_k^0) is replaced by (τ_k) in the following. From this simplified Gibbs relation, we get that the pressure is defined from the internal energy by the relation:

$$P_k(\tau_k) = -\frac{de_k(\tau_k)}{d\tau_k}.$$

It should be noted, that by setting $\rho_k = 1/\tau_k$, we get:

$$\frac{P_k}{\rho_k^2} = \frac{de_k}{d\rho_k}.$$

Moreover, by assuming that $\tau_k \mapsto e_k(\tau_k)$ is strictly convex, we get that the sound speed c_k defined as:

$$c_k^2 = \frac{dP_k}{d\rho_k} = \frac{1}{\rho_k^2}\frac{d^2 e_k}{d{\tau_k}^2},$$

belongs to $\mathbb{R}_+^*$.

2.1 The convective part of the model

Let us present the convective part of the system of equations we are interested in. It models the configurations depicted by figure 1:

$$\begin{cases} \partial_t(\alpha_2) + U_2\partial_x(\alpha_2) = 0, \\ \partial_t(\alpha_1\rho_1) + \partial_x(\alpha_1\rho_1 U_1) = 0, \\ \partial_t(\alpha_1\rho_1 U_1) + \partial_x\big(\alpha_1(\rho_1 U_1^2 + P_1(\tau_1))\big) - \mathcal{P}_I\partial_x(\alpha_1) = 0, \\ \partial_t(\alpha_2\rho_2) + \partial_x(\alpha_2\rho_2 U_2) = 0, \\ \partial_t(\alpha_2\rho_2 U_2) + \partial_x\big(\alpha_2(\rho_2 U_2^2 + P_2(\tau_2))\big) - \mathcal{P}_I\partial_x(\alpha_2) = 0, \end{cases} \tag{1}$$

where we have $\alpha_1 + \alpha_2 = 1$. The pressure $\mathcal{P}_I$ involved in the non-conservative terms are closed according to [8, 9, 10]:

$$\mathcal{P}_I = P_1(\tau_1) - \frac{g\alpha_1 H\rho_1}{2},$$

H corresponds to the total height and it is supposed constant and uniform here, see also figure 1. It should be noted that we consider here the case of an horizontal pipe, but that the model remains meaningful for non horizontal pipes with slope variations. System (1) is written using the set of non-conservative variables $Y = (\alpha_2, \rho 1, U_1, \rho_2, U_2)$ gathering the following variables:

- α_1 which is the fraction of the total height occupied by phase 1, the remaining of the height given by α_2 being occupied by phase 2;
- ρ_k and U_k are respectively the density and the velocity of phase k.

An overview of the associated configurations can be found in figure 1.

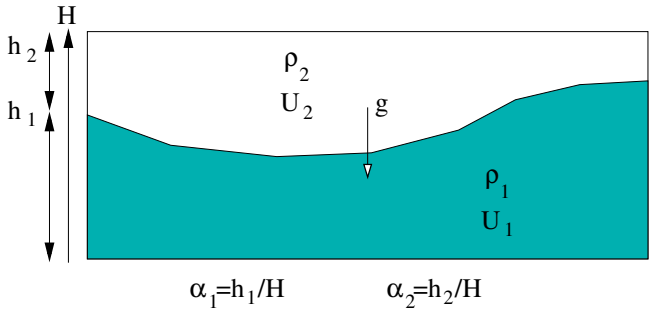

Figure 1: Configuration for the CTL model while considering horizontal pipes.

Let us also define the conservative variables $W = (\alpha_2, m_1, Q_1, m_2, Q_2)$ for which we have set: the partial masses $m_k = \alpha_k \rho_k$ and the momentums $Q_k = m_k U_k$. Considering the variables W system (1) can be equivalently written:

$$\begin{cases} \partial_t(\alpha_2) + Q_2/m_2\ \partial_x(\alpha_2) = 0, \\ \partial_t(m_1) + \partial_x(Q_1) = 0, \\ \partial_t(Q_1) + \partial_x\left(Q_1^2/m_1 + \alpha_1 P_1(\alpha_1/m_1)\right) + \mathcal{P}_I(\alpha_1, m_1)\ \partial_x(\alpha_2) = 0, \\ \partial_t(m_2) + \partial_x(Q_2) = 0, \\ \partial_t(Q_2) + \partial_x\left(Q_2^2/m_2 + \alpha_2 P_2(\alpha_2/m_2)\right) - \mathcal{P}_I(\alpha_1, m_1)\ \partial_x(\alpha_2) = 0. \end{cases} \tag{2}$$

The whole numerical scheme is based on system (2) and the conservative variable W. Such a choice make it more easy to ensure that numerical approximations fulfill balance relations for the mixture. Indeed, it is an important point to quote that since $\alpha_1 + \alpha_2 = 1$, system (2) (and obviously system (1)) leads to a balance equation for the total mass $(m_1 + m_2)$ and for the total momentum $(Q_1 + Q_2)$.

2.2 Accounting for the interfacial exchanges

As in references [8, 9, 10], we choose to define the interfacial source terms that are in agreement with the principle of minimization of a mixture energy (which is the counterpart of the maximization of the entropy of the system). For a study of the convexity of the energy of the isentropic Baer-Nunziato model in a general framework, one may refer to [26]. We first define here the energy of the system: $E = E_1 + E_1^p + E_2$, where E_k is the total energy $E_k = m_k(e_k + U_k^2/2)$ and E_1^p is the potential energy associated with the gravity g, that is: $E_1^p = \alpha_1 m_1 g H/2$. In 7.2 we prove that the energy E is convex (but not strictly convex) with respect the the conservative variables $(\alpha_1, m_1, Q_1, m_2, Q_2)$. For the sake of completeness, the mass transfer is considered in the present section. Nevertheless, the associated source terms will be neglected in the next sections.

System of equations (2) is then supplemented by sources terms:

$$\begin{cases} \partial_t(\alpha_2) + Q_2/m_2\ \partial_x(\alpha_2) = \Phi_2 = -\Phi_1, \\ \partial_t(m_1) + \partial_x(Q_1) = \mathcal{M}_1, \\ \partial_t(Q_1) + \partial_x\left(Q_1^2/m_1 + \alpha_1 P_1(\alpha_1/m_1)\right) + \mathcal{P}_I(\alpha_1, m_1)\ \partial_x(\alpha_2) = \Psi_1, \\ \partial_t(m_2) + \partial_x(Q_2) = -\mathcal{M}_1, \\ \partial_t(Q_2) + \partial_x\left(Q_2^2/m_2 + \alpha_2 P_2(\alpha_2/m_2)\right) - \mathcal{P}_I(\alpha_1, m_1)\ \partial_x(\alpha_2) = -\Psi_1. \end{cases} \tag{3}$$

From system (3), one can obtain that:

$$\begin{array}{l} \partial_t(E) + \partial_x\left(U_1(E_1 + E_1^p + \alpha_1 P_1) + U_2(E_2 + \alpha_2 P_2)\right) = \\ \left(h1 + \frac{\alpha_1 g H}{2} - h_2\right) M_1 + (P_2 - \mathcal{P}_I)\Phi_1 + (U_1 - U_2)\left(\Psi_1 - \frac{U_1+U_2}{2} M_1\right), \end{array} \tag{4}$$

where $h_k = e_k + P_k\tau_k$ denotes the specific enthalpy of phase k. Since the energy of the system E is convex, we intend to choose source terms Φ_1, M_1 and Ψ_1 that decrease the energy and thus that leads to the inequality:

$$\partial_t\left(E\right) + \partial_x\left(U_1(E_1 + E_1^p + \alpha_1 P_1) + U_2(E_2 + \alpha_2 P_2)\right) \leq 0. \tag{5}$$

Concerning the momentum source term Ψ_1, we make the same choice than in [8, 9, 10], that is:

$$\left(\Psi_1 - \frac{U_1 + U_2}{2} M_1\right) = -\lambda_u (U_1 - U_2),$$

or equivalently:

$$\Psi_1 = \overline{V} M_1 - \lambda_u (U_1 - U_2), \tag{6}$$

with $\overline{V} = (U_1 + U_2)/2$ and $\lambda_u \geq 0$. Thanks to the closure (6) for the drag force term, the last term on the right hand side of relation (4) is in agreement with inequality (5). It thus remains to define the source terms M_1 and Φ_1. For the latter, we propose here an other choice that the one introduced in [8, 9, 10]. We follow here the proposition [20]. Three energies are defined:

$$(\alpha_1, m_1) \mapsto \mathcal{E}_0^{\#}(\alpha_1, m_1) = m_1 e_1\left(\frac{\alpha_1}{m_1}\right) + \alpha_1 m_1 \frac{gH}{2} + (m^0 - m_1) e_2\left(\frac{1-\alpha_1}{m^0 - m_1}\right), \tag{7}$$

$$\alpha_1 \mapsto \mathcal{E}_{0,\alpha}^{\#}(\alpha_1) = m_1^0 e_1\left(\frac{\alpha_1}{m_1^0}\right) + \alpha_1 m_1^0 \frac{gH}{2} + m_2^0 e_2\left(\frac{1-\alpha_1}{m^0 - m_1}\right), \tag{8}$$

$$m_1 \mapsto \mathcal{E}_{0,m}^{\#}(m_1) = m_1 e_1\left(\frac{\alpha_1^0}{m_1}\right) + \alpha_1^0 m_1 \frac{gH}{2} + (m^0 - m_1) e_2\left(\frac{\alpha_2^0}{m^0 - m_1}\right). \tag{9}$$

It should be noted that $\mathcal{E}_{0,\alpha}^{\#}(\alpha_1) = \mathcal{E}_0^{\#}(\alpha_1, m_1^0)$ and $\mathcal{E}_{0,m}^{\#}(m_1) = \mathcal{E}_0^{\#}(\alpha_1^0, m_1)$. It can be proved that the energies $\mathcal{E}_{0,\alpha}^{\#}$ and $\mathcal{E}_{0,m}^{\#}$ are strictly convex (see details in 7.2). Moreover, the energy $\mathcal{E}_0^{\#}$ is strictly convex provided that the following sufficient condition is fulfilled:

$$\frac{1}{2}\sqrt{gH} < \min(c_1, c_2). \tag{10}$$

Inequality (10) states that the celerity associated with the gravity waves is smaller that the celerity associated with the thermodynamics (see details in 7.2). It is important to notice that we have:

$$\partial_{\alpha_1}\left(\mathcal{E}_0^{\#}\right) = d_{\alpha_1}\left(\mathcal{E}_{0,\alpha}^{\#}\right) = P_2 - \mathcal{P}_I, \tag{11}$$

and

$$\partial_{m_1}\left(\mathcal{E}_0^{\#}\right) = d_{m_1}\left(\mathcal{E}_{0,m}^{\#}\right) = h_1 - h_2 + \frac{\alpha_1 gH}{2}, \tag{12}$$

and thus that equation (4) for the mixture energy can be written:

$$\begin{array}{l} \partial_t\left(E\right) + \partial_x\left(U_1(E_1 + E_1^p + \alpha_1 P_1) + U_2(E_2 + \alpha_2 P_2)\right) = \\ \partial_{m_1}\left(\mathcal{E}_0^{\#}\right) M_1 + \partial_{\alpha_1}\left(\mathcal{E}_0^{\#}\right)\Phi_1 + (U_1 - U_2)\left(\Psi_1 - \frac{U_1+U_2}{2} M_1\right). \end{array} \tag{13}$$

If we assume that relation (10) holds, it can be deduce from the strict convexity of $\mathcal{E}_0^{\#}$ that for any (α_1, m_1) we have:

$$\forall (\alpha_1', m_1'), \quad \mathcal{E}_0^{\#}(\alpha_1', m_1') \geq \mathcal{E}_0^{\#}(\alpha_1, m_1) + \partial_{m_1}\left(\mathcal{E}_0^{\#}\right)(\alpha_1, m_1)(m_1' - m_1) + \partial_{\alpha_1}\left(\mathcal{E}_0^{\#}\right)(\alpha_1, m_1)(\alpha_1' - \alpha_1). \tag{14}$$

Moreover, there exists a unique minimizer $(\overline{\alpha_1}, \overline{m_1})$ such that:

$$\forall (\alpha_1, m_1), \quad \mathcal{E}_0^{\#}(\overline{\alpha_1}, \overline{m_1}) \leq \mathcal{E}_0^{\#}(\alpha_1, m_1).$$

Hence, equation (14) gives for $(\alpha_1', m_1') = (\overline{\alpha_1}, \overline{m_1})$:

$$\forall (\alpha_1, m_1), \quad \partial_{m_1}\left(\mathcal{E}_0^{\#}\right)(\alpha_1, m_1)(\overline{m_1} - m_1) + \partial_{\alpha_1}\left(\mathcal{E}_0^{\#}\right)(\alpha_1, m_1)(\overline{\alpha_1} - \alpha_1) \leq \mathcal{E}_0^{\#}(\overline{\alpha_1}, \overline{m_1}) - \mathcal{E}_0^{\#}(\alpha_1, m_1) \leq 0. \tag{15}$$

Therefore, for ensuring inequality (5), one possible modeling choice for the mass transfer term M_1 and for the pressure relaxation term Φ_1 is:

$$M_1 = \lambda_{mp}\left(\overline{m_1} - m_1\right) \quad \text{and} \quad \Phi_1 = \lambda_{mp}\left(\overline{\alpha_1} - \alpha_1\right), \tag{16}$$

where λ_{mp}^{-1} is a positive time scale. If one excludes single phase situations, i.e. $\alpha_1 \in]0,1[$, then the minimizer $(\overline{\alpha_1}, \overline{m_1})$ is defined as the unique point for which the derivatives of the energy $\mathcal{E}_0^{\#}$ with respect to α_1 and m_1 vanish. Thanks to relations (11), (12) and to the definition of $\mathcal{P}_I$ this yields:

$$\left\{ \begin{array}{l} P_2\left(\frac{(m_1^0+m_2^0)-\overline{m_1}}{1-\overline{\alpha_1}}\right) = P_1\left(\frac{\overline{m_1}}{\overline{\alpha_1}}\right) - \frac{\overline{m_1}gH}{2}, \\ h_1\left(\frac{\overline{m_1}}{\overline{\alpha_1}}\right) = h_2\left(\frac{(m_1^0+m_2^0)-\overline{m_1}}{1-\overline{\alpha_1}}\right) + \frac{\overline{\alpha_1}gH}{2}. \end{array} \right. \tag{17}$$

Despite the model can handle mass transfer, it is not accounted for in the following. We restrict in the next sections to liquid-gas flows that are only subject to pressure relaxation and to velocity relaxation.

3 Numerical method

As mentioned in the introduction, we intend to develop a scheme that solves some of the physical effects in a coupled manner. We thus develop here a very classical approach based on Chorin's idea. System (2) is split into three subsystems that are then solved sequentially, see section 3.1. The main advantage of such methods is that they allow to overcome the classical CFL limitation based on the VNL waves for the explicit schemes. Moreover, staggered meshes are used for discretizing the spatial derivatives, see 3.2. Actually, the global scheme corresponds to the classical MAC scheme.

3.1 A fractional step approach for the time-stepping

System (2) is split into three sub-systems (18), (19) and (20). The first sub-system concerns the prediction of the momentums while the fractions and the partial masses remain constant:

$$\left\{ \begin{array}{l} \partial_t(\alpha_2) = 0, \\ \partial_t(m_1) = 0, \\ \partial_t(Q_1) + \partial_x(U_1(t=0)Q_1 + \alpha_1 P_1) + \mathcal{P}_I\ \partial_x(\alpha_2) = \lambda_u(t=0)\left(\frac{\alpha_2 Q_2}{m_2} - \frac{\alpha_1 Q_1}{m_1}\right), \\ \partial_t(m_2) = 0, \\ \partial_t(Q_2) + \partial_x(U_2(t=0)Q_2 + \alpha_2 P_2) - \mathcal{P}_I\ \partial_x(\alpha_2) = -\lambda_u(t=0)\left(\frac{\alpha_2 Q_2}{m_2} - \frac{\alpha_1 Q_1}{m_1}\right). \end{array} \right. \tag{18}$$

It should be noted that the fractions α_k and the partial masses m_k - and thus the densities ρ_k - are constant in this first step (18). Moreover, the parameter for velocity relaxation λ_u is frozen at initial time. The second sub-system focuses on the mass equation and accounts for a part of the momentum equation. The fractions remain constant. This step corresponds to the so-called pressure-correction step.

$$\left\{ \begin{array}{l} \partial_t(\alpha_2) = 0, \\ \partial_t(m_1) + \partial_x(Q_1) = 0, \\ \partial_t(Q_1) + \partial_x(\alpha_1(P_1 - P_1(t=0))) + (\mathcal{P}_I - \mathcal{P}_I(t=0))\ \partial_x(\alpha_2) = 0, \\ \partial_t(m_2) + \partial_x(Q_2) = 0, \\ \partial_t(Q_2) + \partial_x(\alpha_2(P_2 - P_2(t=0))) - (\mathcal{P}_I - \mathcal{P}_I(t=0))\ \partial_x(\alpha_2) = 0. \end{array} \right. \tag{19}$$

At last, the third subsystem only deals with the advection of the fractions and on the pressure relaxation source term:

$$\left\{ \begin{array}{l} \partial_t(\alpha_2) + Q_2/m_2\ \partial_x(\alpha_2) = \lambda_{mp}(t=0)(\overline{\alpha_2} - \alpha_2), \\ \partial_t(m_1) = 0, \\ \partial_t(Q_1) = 0, \\ \partial_t(m_2) = 0, \\ \partial_t(Q_2) = 0, \end{array} \right. \tag{20}$$

where $\overline{\alpha_2} = 1 - \overline{\alpha_1}$. As for the drag force in the first substep, the parameter for pressure relaxation λ_{mp} is frozen at initial time. Each of these three substeps are then discretized using an implicit Euler scheme for a given time-step Δt. Let us denote by W^n the approximated value at the beginning of the current time-iteration. The first step associated with system (18) then produces the approximated value W^* such that:

$$\left\{ \begin{array}{l} \alpha_2^* = \alpha_2^n, \\ m_1^* = m_1^n, \\ Q_1^* - Q_1^n + \Delta t\ \partial_x(U_1^n Q_1^* + \alpha_1^n P_1^n) + \Delta t\ \mathcal{P}_I^n\ \partial_x(\alpha_2^n) = \lambda_u^n\left(\frac{\alpha_2^n Q_2^*}{m_2^n} - \frac{\alpha_1^n Q_1^*}{m_1^n}\right), \\ m_2^* = m_2^n, \\ Q_2^* - Q_2^n + \Delta t\ \partial_x(U_2^n Q_2^* + \alpha_2^n P_2^n) - \Delta t\ \mathcal{P}_I^n\ \partial_x(\alpha_2^n) = -\lambda_u^n\left(\frac{\alpha_2^n Q_2^*}{m_2^n} - \frac{\alpha_1^n Q_1^*}{m_1^n}\right), \end{array} \right. \tag{21}$$

where $P_k^n = P_k(m_k^n/\alpha_k^n)$ and $\mathcal{P}_I^n = \mathcal{P}_I(\alpha_k^n, m_k^n)$. It should be noted that sole the momentums Q_k are not explicitly known in (21). Moreover, when the drag force is not accounted for, Q_1^n and Q_2^n can be solved independently. For the second step, system (19) is solved at time $t = \Delta t$ with W^* as an initial condition. The implicit Euler scheme then leads to the approximated solution $W^\#$:

$$\left\{\begin{array}{l} \alpha_2^\# = \alpha_2^*, \\ m_1^\# - m_1^* + \Delta t\ \partial_x\left(Q_1^\#\right) = 0, \\ Q_1^\# - Q_1^* + \Delta t\ \partial_x\left(\alpha_1^*(P_1^\# - P_1^*)\right) + \Delta t\ \left(\mathcal{P}_I^\# - \mathcal{P}_I^*\right)\ \partial_x\left(\alpha_2^*\right) = 0, \\ m_2^\# - m_2^* + \Delta t\ \partial_x\left(Q_2^\#\right) = 0, \\ Q_2^\# - Q_2^* + \Delta t\ \partial_x\left(\alpha_2^*(P_2^\# - P_2^*)\right) - \Delta t\ \left(\mathcal{P}_I^\# - \mathcal{P}_I^*\right)\ \partial_x\left(\alpha_2^*\right) = 0, \end{array}\right. \tag{22}$$

where $P_k^* = P_k(m_k^*/\alpha_k^*)$, $\mathcal{P}_I^* = \mathcal{P}_I(\alpha_k^*, m_k^*)$, $P_k^\# = P_k(m_k^\#/\alpha_k^\#)$ and $\mathcal{P}_I^\# = \mathcal{P}_I(\alpha_k^\#, m_k^\#)$. System of equations (22) is classically linearized in the following way. Since we are dealing with isentropic phases, the sound speed c_k is defined as:

$$c_k^2 = \partial_{\rho_k}\left(P_k\right).$$

We thus define the pressure increment $\delta P_k = P_k^\# - P_k^*$ and the mass increment are then linearized:

$$m_k^\# - m_k^* = \alpha_k^*(\rho_k^\# - \rho_k^*) \sim \alpha_k^* \frac{\delta P_k}{(c_k^*)^2}. \tag{23}$$

The term containing the pressure interface is also linearized by the formula:

$$\mathcal{P}_I^\# - \mathcal{P}_I^* \sim \left(1 - \frac{\alpha_1^* g H}{2(c_1^*)^2}\right)\delta P_1 = \beta^* \delta P_1,$$

with the definition:

$$\beta^* = \left(1 - \frac{\alpha_1^* g H}{2(c_1^*)^2}\right).$$

Then by introducing the third equation of (22) into the second one, we obtain an equation that only involves δP_1:

$$\alpha_1^* \frac{\delta P_1}{\Delta t (c_1^*)^2} + \partial_x\left(Q_1^*\right) - \Delta t\ \partial_{xx}^2\left(\alpha_1^* \delta P_1\right) + \Delta t\ \beta^* \partial_x\left(\delta P_1 \partial_x\left(\alpha_1^*\right)\right) + \Delta t \delta P_1 \partial_x\left(\beta^*\right)\partial_x\left(\alpha_1^*\right) = 0 \tag{24}$$

In the same way, when introducing the fifth equation of (22) into the forth one, one obtain an equation for δP_1 and δP_2:

$$\alpha_2^* \frac{\delta P_2}{\Delta t (c_2^*)^2} + \partial_x\left(Q_2^*\right) - \Delta t\ \partial_{xx}^2\left(\alpha_1^* \delta P_2\right) - \Delta t\ \beta^* \partial_x\left(\delta P_1 \partial_x\left(\alpha_1^*\right)\right) - \Delta t \delta P_1 \partial_x\left(\beta^*\right)\partial_x\left(\alpha_1^*\right) = 0 \tag{25}$$

It should be mentioned that the last term in equation (24) and (25) arises from the decomposition of the derivative of the product $\beta^* \delta P_1 \partial_x\left(\alpha_1^*\right)$:

$$\partial_x\left(\beta^* \delta P_1 \partial_x\left(\alpha_1^*\right)\right) = \beta^* \partial_x\left(\delta P_1 \partial_x\left(\alpha_1^*\right)\right) + \delta P_1 \partial_x\left(\beta^*\right)\partial_x\left(\alpha_1^*\right).$$

Once these two equations are solved, the partial masses are updated following equation (23):

$$m_k^\# = m_k^* + \alpha_k^* \frac{\delta P_k}{(c_k^*)^2},$$

and the momentums are updated according to the third and fifth equations of system (22). The last step of the algorithm, which corresponds to sub-system (20), gives the updated values W^{n+1} with $W^\#$ as an initial condition. It reads:

$$\left\{\begin{array}{l} \alpha_2^{n+1} - \alpha_2^\# + \Delta t (Q_2/m_2)^\#\ \partial_x\left(\alpha_2^{n+1}\right) = \lambda_{mp}^\#(\overline{\alpha_2}^\# - \alpha_2^{n+1}), \\ m_1^{n+1} = m_1^\#, \\ Q_1^{n+1} = Q_1^\#, \\ m_2^{n+1} = m_2^\#, \\ Q_2^{n+1} = Q_2^\#. \end{array}\right. \tag{26}$$

Putting together the three sets of equations (21), (22) and (26), one gets the following system:

$$\left\{\begin{array}{l} \frac{\alpha_2^{n+1}-\alpha_2^n}{\Delta t} + (Q_2/m_2)^{n+1}\ \partial_x\left(\alpha_2^{n+1}\right) = \lambda_{mp}^{\#}(\overline{\alpha_2}^n - \alpha_2^{n+1}), \\ \frac{m_1^{n+1}-m_1^n}{\Delta t} + \partial_x\left(Q_1^{n+1}\right) = 0, \\ \frac{Q_1^{n+1}-Q_1^n}{\Delta t} + \partial_x\left(U_1^n Q_1^* + \alpha_1^{\#} P_1^{\#}\right) + \Delta t\ \mathcal{P}_I^{\#}\ \partial_x\left(\alpha_2^{\#}\right) = \lambda_u^n\left(\frac{\alpha_2^n Q_2^*}{m_2^n} - \frac{\alpha_1^n Q_1^*}{m_1^n}\right), \\ \frac{m_2^{n+1}-m_2^n}{\Delta t} + \partial_x\left(Q_2^{n+1}\right) = 0, \\ \frac{Q_2^{n+1}-Q_2^n}{\Delta t} + \partial_x\left(U_2^n Q_2^* + \alpha_2^{\#} P_2^{\#}\right) - \Delta t\ \mathcal{P}_I^{\#}\ \partial_x\left(\alpha_2^{\#}\right) = -\lambda_u^n\left(\frac{\alpha_2^n Q_2^*}{m_2^n} - \frac{\alpha_1^n Q_1^*}{m_1^n}\right). \end{array}\right. \tag{27}$$

The approximation of the solution through the scheme proposed here is thus a first-order scheme in time. First equation of system (27) allows a strong coupling between convective effects and pressure relaxation in the computation of the fraction α_2. It now remains to explain how the space-derivative terms are approximated.

Remark. It is an important point to be quoted that the first equation of system (26) is linear with respect to α_2^{n+1}. This is due to the new form of pressure relaxation source term proposed here. Indeed, in the original model [8, 9, 10], equation for the fraction α_2 reads:

$$\partial_t(\alpha_2) + U_2\partial_x(\alpha_2) = \lambda_{mp}\left(P_2(m_2/\alpha_2) - P_1(m_1/\alpha_1) + \frac{m_1 gH}{2}\right). \tag{28}$$

Hence, when the phasic pressures are non-linear with respect to α_2, the discretization of equation (28) through the last step (20) of the time algorithm (i.e. the equation corresponding to the first equation of system (26)) would lead to the following non-linear equation:

$$\alpha_2^{n+1} - \alpha_2^{\#} + \Delta t(Q_2/m_2)^{\#}\ \partial_x\left(\alpha_2^{n+1}\right) = \lambda_{mp}^{\#}\left(P_2\left(\frac{m_2^{\#}}{\alpha_2^{n+1}}\right) - P_1\left(\frac{m_1^{\#}}{1-\alpha_2^{n+1}}\right) + \frac{m_1^{\#} gH}{2}\right). \tag{29}$$

Depending on the pressure laws, equation (29) can be tricky to solve. This is even more true when including the space-derivative discretization which implies to solve a non-linear system of equations that couples all the cell-values (see section 3.2). On the contrary, with the modified source term which is linear in α_2, the non-linearity of the pressure laws only arises in the computation of the equilibrium fraction $\overline{\alpha_2}$ which is performed cell-wise and thus involves a sole non-linear equation for each cell.

3.2 Spacial discretization on staggered meshes

The spatial derivatives in the subsystems introduced in section 3 are approximated using a first order finite volume scheme on staggered meshes. Since the time stepping algorithm is first order, and due to the Lie-Trotter splitting associated with the fractional step approach of section 3.1, it can not be expected an order greater than 1 for the whole scheme. We thus use here a first-order space-derivative discretization. We consider that the primal mesh is associated with the "thermodynamical" quantities: α_2 and m_k, whereas the dual mesh is associated with the momentums Q_k. Cell i of the primal mesh is the interval $[x_i, x_{i+1}]$ with $x_{i+1} = x_i + L_i$. Then cell i of the dual mesh is "centered" on the left boundary of the cell i of the primal mesh: it corresponds to the interval $[x_i - L_{i-1}/2, x_i + L_i/2]$, which has thus a length $\widetilde{L}_i = L_{i-1}/2 + L_i/2$. We also define the following mean quantities on the cell i of the primal mesh:

$$\alpha_{k,i}^{n+1} = \frac{1}{L_i}\int_{x_i}^{x_{i+1}} \alpha_k^{n+1}(x)dx, \quad \text{and} \quad m_{k,i}^{n+1} = \frac{1}{L_i}\int_{x_i}^{x_{i+1}} m_k^{n+1}(x)dx,$$

and on cell i of the dual mesh:

$$Q_{k,i}^{n+1} = \frac{1}{\widetilde{L}_i}\int_{x_i - L_{i-1}/2}^{x_i + L_i/2} Q_k^{n+1}(x)dx.$$

A sketch of all these notations is proposed in figure 2.

Let us start by the first step, i.e. by system (21). The momentum equation for phase k in cell i is approximated by the formula:

$$\begin{array}{rcl} Q_{k,i}^* + \Delta t\frac{U_{k,i+1/2}^n Q_{k,i+1/2}^* - U_{k,i-1/2}^n Q_{k,i-1/2}^*}{\widetilde{L}_i} & = & \\ Q_{k,i}^n - \Delta t\frac{\alpha_{k,i}^n P_{k,i}^n - \alpha_{k,i-1}^n P_{k,i-1}^n}{\widetilde{L}_i} & + & \Delta t\widetilde{P}_I^n\ \frac{\alpha_{k,i}^n - \alpha_{k,i-1}^n}{\widetilde{L}_i}, \end{array} \tag{30}$$

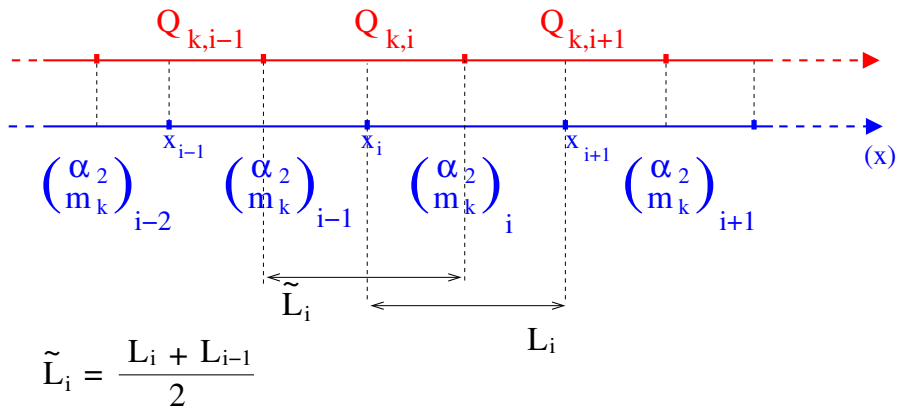

Figure 2: Notations and settings of the staggered meshes: the primal mesh is in blue, and the dual mesh is in red.

where the momentum flux is defined as an Upwind flux:

$$Q^*_{k,i-1/2} = \begin{cases} Q^*_{k,i} & \text{if} \quad U^n_{k,i-1/2} < 0, \\ Q^*_{k,i-1} & \text{otherwise,} \end{cases}$$

with $U^n_{k,i-1/2} = (Q^n_{k,i} + Q^n_{k,i-1})/(2\rho^n_{k,i-1})$. The interfacial pressure term $\widetilde{P}^n_I$ is:

$$\widetilde{P}^n_I = \frac{P_1(\rho^n_{1,i}) + P_1(\rho^n_{1,i-1})}{2} - \frac{gH}{2}\frac{L_i m^n_{1,i} + L_{i-1} m^n_{1,i-1}}{L_i + L_{i-1}}.$$

In equation (30) the right hand side is explicitly known and the left hand side contains all the unknown $Q^*_{k,i}$. Thanks to the Upwind choice which is semi-implicit, equation (30) is linear in terms of the momentums $Q^*_{k,i}$.

The second step (22) is more complex since it couples the mass equations and simplified momentum equations. We first focus on equation (24). It contains second order derivatives in space, the latter are discretized by the formula proposed in 7.1. According to this formula, and in order to build a linear system for the unknowns $\delta P_{1,i}$, the term $\partial_x\left(\delta P_1 \partial_x\left(\alpha^*_1\right)\right)$ is replaced by $\partial^2_{xx}\left(\alpha^*_1 \delta P_1\right) - \partial_x\left(\alpha^*_1 \partial_x\left(\delta P_1\right)\right)$ and (24) is discretized in the form:

$$\alpha^*_1 \frac{\delta P_1}{\Delta t (c^*_1)^2} + \partial_x\left(Q^*_1\right) + \Delta t\ (1-\beta^*)\partial^2_{xx}\left(\alpha^*_1 \delta P_1\right) + \Delta t\ \beta^* \partial_x\left(\alpha^*_1 \partial_x\left(\delta P_1\right)\right) + \Delta t \delta P_1 \partial_x\left(\beta^*\right)\partial_x\left(\alpha^*_1\right) = 0 \tag{31}$$

Then, equation (31) leads to:

$$\begin{array}{ll} \delta P_{1,i}\left(\frac{\alpha^*_{1,i}}{\Delta t (c^*_{1,i})^2} + \Delta t \partial_x\left(\beta^*_i\right)\partial_x\left(\alpha^*_{1,i}\right)\right) & +\Delta t\ (1-\beta^*_i)\partial^2_{xx}\left(\alpha^*_{1,i}\delta P_{1,i}\right) \\ & +\Delta t\ \beta^*_i \partial_x\left(\alpha^*_{1,i}\partial_x\left(\delta P_{1,i}\right)\right) \quad = -\frac{Q^*_{1,i+1} - Q^*_{1,i}}{L_i}, \end{array} \tag{32}$$

where the second derivative terms can be found in (7.1). The two derivatives arising in the first term of equation (32) are explicit. They involve β^* and $\alpha^*_{1,i}$ and are approximated using a centered formula in cell i:

$$\partial_x\left(\phi_i\right) \sim \frac{1}{L_i}\left(\frac{L_{i+1}\phi_{i+1} + L_i\phi_i}{L_{i+1} + L_i} - \frac{L_i\phi_i + L_{i-1}\phi_{i-1}}{L_i + L_{i-1}}\right).$$

Therefore, equation (32) leads to a linear system whith the unknowns $\delta P_{1,i}$. The mass equation for phase 2 is discretized using the same recipes and it also leads to a linear system, but the latter involves both $\delta P_{1,i}$ and $\delta P_{2,i}$. Once these linear systems are solved, the partial masses and the momentums can be updated according to (23) and to the third and fifth equations of system (22). That is we have for the partial masses:

$$m^{\#}_{k,i} = m^*_{k,i} + \alpha^*_{k,i}\frac{\delta P_{k,i}}{(c^*_{k,i})^2}, \tag{33}$$

and for the momentums:

$$Q^{\#}_{k,i} = Q^*_{k,i} - \Delta t\ \frac{\alpha^*_{k,i}\delta P_{k,i} - \alpha^*_{k,i-1}\delta P_{k,i-1}}{\widetilde{L}_i} - \Delta t\ \beta^*_i\ \delta\overline{P}_{1,i}\partial_x\left(\alpha^*_{k,i}\right), \tag{34}$$

with $\delta\overline{P}_{1,i} = (L_i\delta P_{1,i} + L_{i-1}\delta P_{1,i-1})/(L_i + L_{i-1})$. Updates (33) and (34) are explicit and they do not require to solve a linear system.

Remark. The update of the partial masses through equation (33) is mandatory in order to maintain the mass conservation during the simulation of transients. This update is often replaced by an update that involves the EOS: $m^{\#}_{k,i} = \alpha^{\#}_{k,i}\rho_k(P^*_{k,i} + \delta P_k)$; and that does not ensure mass conservation for transient simulations. Obviously, with such an update, the approximate solutions computed by the whole scheme can not converge towards the correct solution if it involves shock waves. Therefore, update (33) has been retained here for the partial masses.

At last, third step (26) only involves the fraction. It is based on an Upwind scheme adapted to the non-conservative framework. It must be emphasized, that U_2 is a Riemann invariant in the linearly degenerate wave associated with the fraction. Hence, considering analytical solutions, the velocity U_2 is locally uniform when the fraction is discontinuous. We first define a local velocity:

$$\widetilde{U}_{2,i} = \frac{Q^{\#}_{2,i} + Q^{\#}_{2,i+1}}{2\ \rho^{\#}_{2,i}}.$$

An upwind choice is then applied foe the derivative term in first equation of (26), that is:

$$\alpha^{n+1}_{2,i} = \alpha^{\#}_{2,i} - \frac{\Delta t}{L_i}\widetilde{U}_{2,i}\ \delta\alpha^{n+1}_{2,i}, \tag{35}$$

where

$$\delta\alpha^{n+1}_{2,i} = \begin{cases} \alpha^{n+1}_{2,i+1} - \alpha^{n+1}_{2,i} & \text{if} \quad \widetilde{U}_{2,i} < 0, \\ \alpha^{n+1}_{2,i} - \alpha^{n+1}_{2,i-1} & \text{otherwise.} \end{cases}$$

With these choices, (35) gives a linear system with unknowns $\alpha^{n+1}_{2,i}$.

In this work, all the linear systems are solved using the Gauss-Seidel method with a sparse matrix storage. Only the diagonal parts of the matrix are stored. In order to limit the spreading of the extra-diagonal terms due to the coupling terms, a special arrangement of the phases is used. In the following, the stopping criterion for the Gauss-Seidel algorithm is based on a threshold between two successive approximate solutions. The error is measured in terms of the L^1-norm divided by the number of primal cells in the mesh: $\sum_{i=1}^{i=N} |X^l_i - X^{l+1}_i|/N < \epsilon$. A threshold of $\epsilon = 10^{-12}$ has been used for the numerical tests of the sections below. It should be noted that provided that the time-step remains small (namely for CFL_{u+c} numbers not too large), the matrices arising from the different steps are diagonally dominant and the Gauss-Seidel method is thus stable. In a practical point of view, no trouble has been encountered during the tests presented in the next sections even for very large CFL_{u+c} numbers.

The time-step Δt is estimated at the beginning of each time-iteration on the basis of the maximum of the speed of the pressure waves $U \pm c$. The latter is computed using the values in the cells (primal and dual) of the approximated solution at the previous time-iteration.

4 Verification test case

We propose in this section to test the numerical method described in section 3 on a class of Riemann problems that only involves shock waves and a contact discontinuity wave. The wave configuration of this class of Riemann problems is depicted in figure 3. Two sets of EOS are used in the following. In section 4.1 we follow [8, 9, 10] and a Riemann problem is built on the basis of a linear law for the liquid and a perfect gas EOS for the gas. In section 4.2, both liquid and gas are described by the mean of a Stiffened Gas EOS adapted to the isentropic setting.

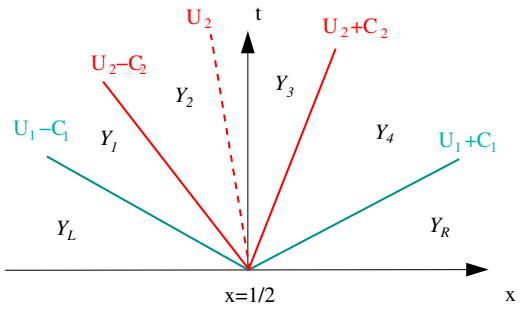

Figure 3: Configuration of the different waves for the Riemann problem: $U_k \pm c_k$-waves are shocks whereas the U_2-wave is obviously a contact discontinuity. The initial discontinuity between left and right states, respectively Y_L and Y_R, is located at $x = 1/2$.

4.1 Linear EOS for the liquid and perfect gas EOS for the gas

As in [8, 9, 10], we consider here a linear law for phase 1 and a perfect gas law for phase 2:

$$P_1(\rho_1) = C_{1,ref}^2(\rho_1 - \rho_{1,ref}) + P_{1,ref},$$

$$\text{with} \quad C_{1,ref} = 1500\ m/s, \quad \rho_{1,ref} = 998.1115\ kg/m^3, \quad P_{1,ref} = 1.0133e5\ Pa;$$

$$P_2(\rho_2) = P_{2,ref}\left(\frac{\rho_2}{\rho_{2,ref}}\right)^{\gamma_2},$$

$$\text{with} \quad P_{2,ref} = 1.01325e5\ Pa, \quad \rho_{2,ref} = 1.204\ kg/m^3, \quad \gamma_2 = 1.4.$$

The total height H is set to 1. The intermediate states Y_m, $m \in \{1, 2, 3, 4\}$, Y_L and Y_R, defining the Riemann problem considered here are gathered in table 1. We consider the final time $t_{end} = 2.3\ 10^{-4}\ s$. Convergence curves are plotted in figure 4 for meshes containing from 100 to 100000 cells. It should be noted from figure 4 that the expected asymptotic rate of convergence of 1/2 has been recovered for all the variables. The approximated solution obtained for a mesh containing 1000 cells is plotted in figure 6 for a CFL_{u+c} number of 0.5. Figure 5 presents the error for a mesh containing 1000 cells for a CFL_{u+c} number between 0.05 and 100. It clearly arises from these results that, even if the scheme can handle large CFL_{u+c} numbers, the optimal CFL_{u+c} number regarding the accuracy of the approximated solutions is around 0.5. Moreover, it should be noted that increasing the CFL_{u+c} number for a given simulation and for a given mesh size can lead to an increase of the computational time. Indeed, for a large CFL_{u+c} number the value of the time-step is bigger and it is thus required less time-iteration. But, for each time-iteration, the computation of the solution of the different linear systems through the Gauss-Seidel method then requires more iterations.

	α_2	$\rho_1\ (kg/m^3)$	$U_1\ (m/s)$	$\rho_2\ (kg/m^3)$	$U_2\ (m/s)$
Y_L	0.5	998.111500000000	10	1.204	5
Y_1	0.5	998.161101784576	9.9254584	1.204	5
Y_2	0.5	998.161101784576	9.9254584	1.26422702503085	−11.83896
Y_3	0.4976253	998.16208780496	9.82255768821687	1.26012920420671	−11.83896
Y_4	0.4976253	998.16208780496	9.82255768821687	1.23491558633234	−18.826134
Y_R	0.4976253	998.062877627989	9.673461	1.23491558633234	−18.826134

Table 1: Linear/perfect gas EOS: Intermediate states for the Riemann problem.

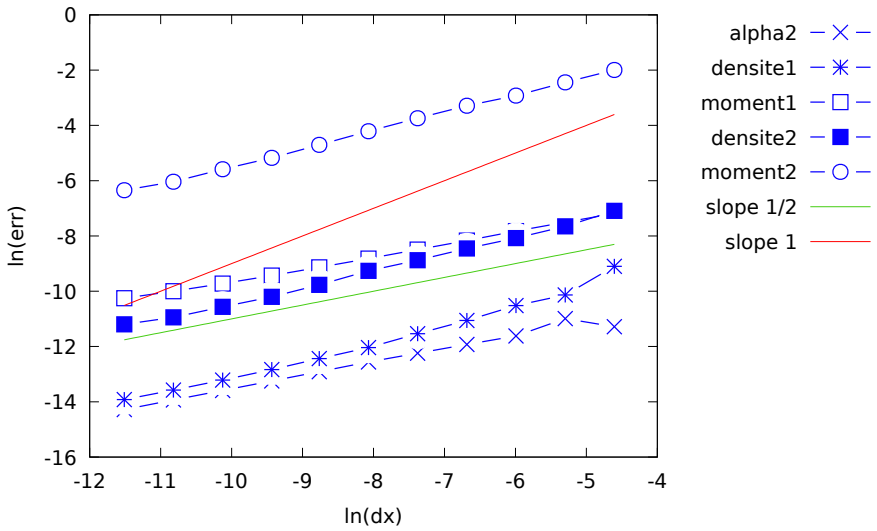

Figure 4: Linear/perfect gas EOS: Convergence curves for meshes containing from 100 to 100000 cells.

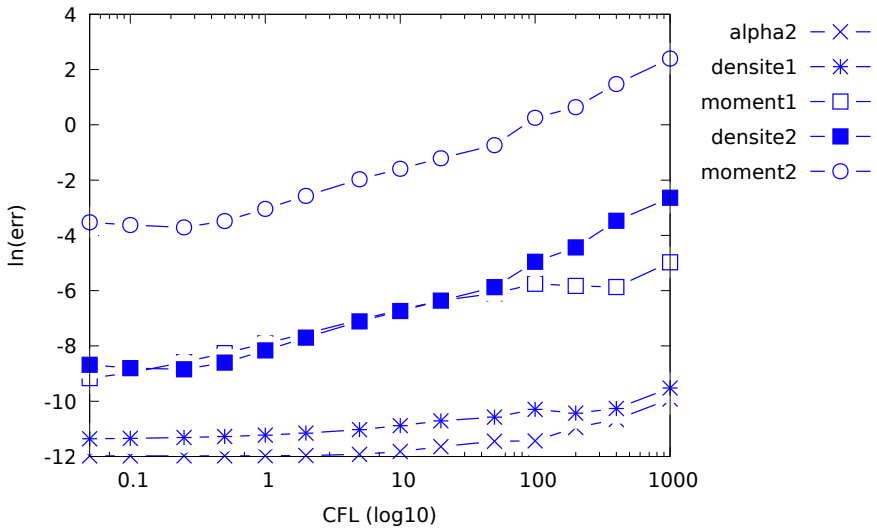

Figure 5: Linear/perfect gas EOS: Error with respect to the CFL_{u+c} number for a mesh containing 1000 cells. CFL_{u+c} number are between 0.05 and 1000.

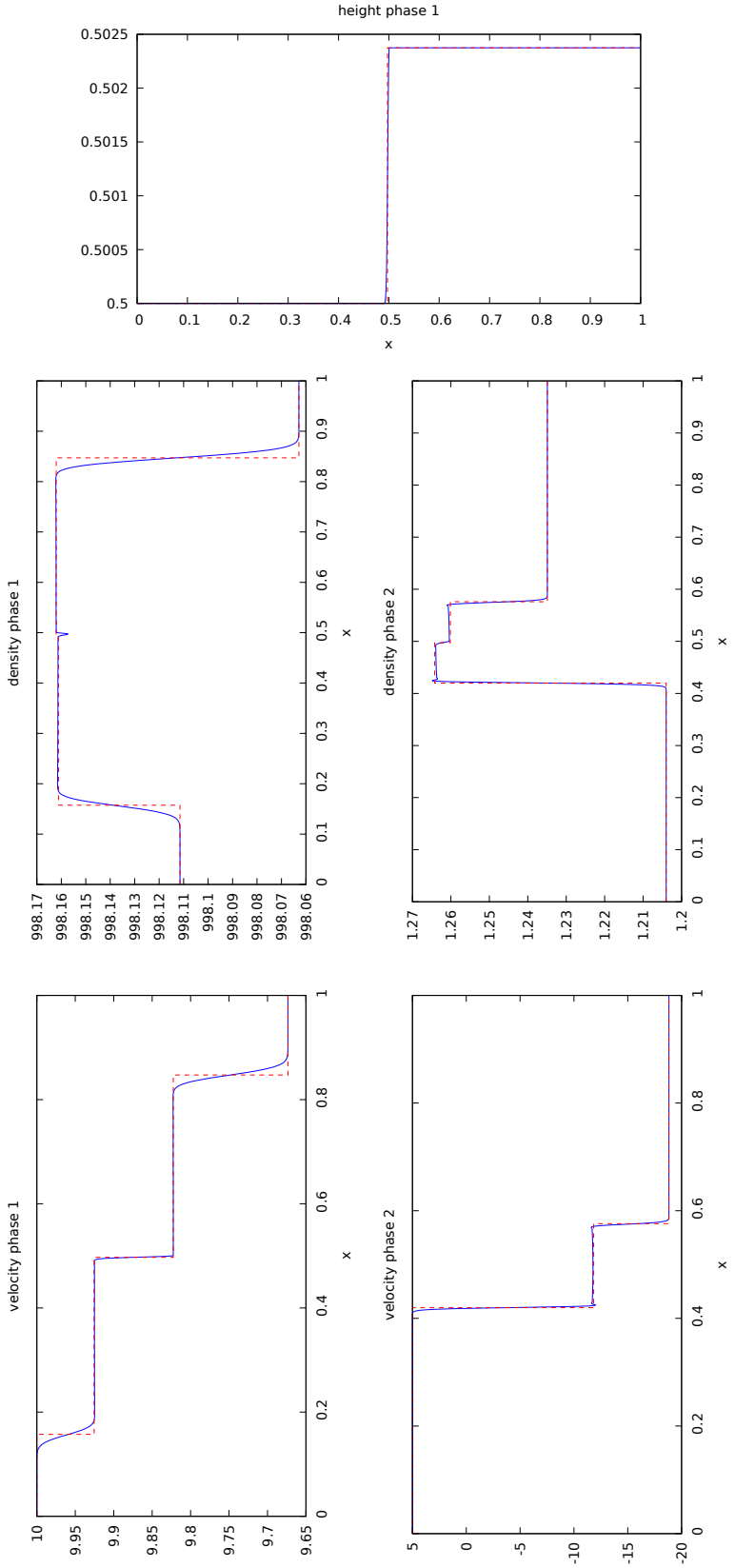

Figure 6: Linear/perfect gas EOS: Results for ρ_k and U_k for a mesh with 1000 cells and a CFL_{u+c} equal to 0.5 (blue lines), and the exact solution (red dashed line).

4.2 Stiffened Gas EOS for both the liquid and the gas

For the present test case, we consider for each phase the isentropic Stiffened Gas EOS:

$$e_k(\rho_k) = E_k^0 + \frac{K_k^0}{\gamma_k - 1}\rho_k^{(\gamma_k - 1)} + \Pi_k/\rho_k,$$

where the parameters E_k^0, K_k^0, γ_k and Π_k have to be given by the user. In this section, the parameters are chosen to be representative of liquid/gas flows at a pressure of 10^5 Pa. They are:

$$\gamma_1 = 1.01,\ \Pi_1 = 2266859575.19171,\ E_1^0 = -238424735.727836,\ K_1^0 = 2207867.96011974,$$

for the liquid phase, and:

$$\gamma_2 = 1.4,\ \Pi_2 = -3690.36462816385,\ E_2^0 = -1.39648879786521e+05,\ K_2^0 = 196527.481874903,$$

for the gas. We still set $H = 1$, as in the previous test case. The four intermediate states Y_m, $m \in \{1, 2, 3, 4\}$, Y_L and Y_R, defining the Riemann problem considered here can be found in table 2. We consider the final time $t_{end} = 2.0\ 10^{-4}\ s$.

	α_2	$\rho_1\ (kg/m^3)$	$U_1\ (m/s)$	$\rho_2\ (kg/m^3)$	$U_2\ (m/s)$
Y_L	0.501	958.636889676032	0.15	0.590332024707516	20
Y_1	0.501	958.655498720767	0.12	0.590332024707516	20
Y_2	0.501	958.655498720767	0.12	0.602943609739854	10
Y_3	0.499	958.655650884766	0.159442679721353	0.602197909093262	10
Y_4	0.499	958.655650884766	0.159442679721353	0.595871603800381	5
Y_R	0.499	958.618778845545	0.1	0.595871603800381	5

Table 2: Two perfect gas EOS: Intermediate states for the Riemann problem.

The same remarks than that for the test case of section 4.1 hold. The convergence curves are plotted in figure 7, the approximated solution for a mesh with 1000 cells is plotted in figure 10, and the curves showing the error with respect to the CFL number at a given mesh size may be found in figure 8.

We insist here on a specific point that is more significant for the stiffened gas EOS and that can first be observed in figure 8. One can clearly note that for the fraction α_2, the error with respect to the CFL_{u+c} number reaches a minimum for a value of the CFL_{u+c} number around 150. In fact, the latter corresponds to a time step associated with the contact wave for α_2. Indeed, the contact wave travels with a speed around 10 m/s (the exact speed of the contact wave is $10m/s$) while pressure waves travel in the liquid phase at the sound speed:

$$\sqrt{\left(\gamma_1 K_1^0 \rho_1^{\gamma_1 - 1}\right)} \sim 1540\ m/s,$$

see figure 10. Thus the ratio between the speed of liquid pressure waves and the contact wave is around $1540/10 = 154$. In order to give an other point of view of that behavior, the CPU-time has been plotted versus the error in figure 9 for different CFL_{u+c} numbers ranging in $[0.05, 1000]$. In figure 9, for each variable, the CFL_{u+c} number increases when following the arrows. These curves clearly show that when considering the whole set of variables, the best choice in terms of efficiency is clearly to get a CFL_{u+c} number close to 1. Nevertheless, the efficiency for the variable α_2 behaves in a very particular manner. We recall that α_2 is the only variable that does not depend on the density waves. When the CFL_{u+c} number increases, the error remains almost constant and for a CFL_{u+c} number of 150 it even becomes lower than the error for a CFL_{u+c} equal to 1. This has also been observed above in figure 8. Nevertheless, figure 9 shows that the CPU-time for CFL_{u+c} number of 150 is far more important than for a CFL_{u+c} number close to 1. **Hence, at least for this test case, a CFL_{u+c} number close to 1 seems to be an optimal choice to get an accurate approximated solution within a low CPU-time.**

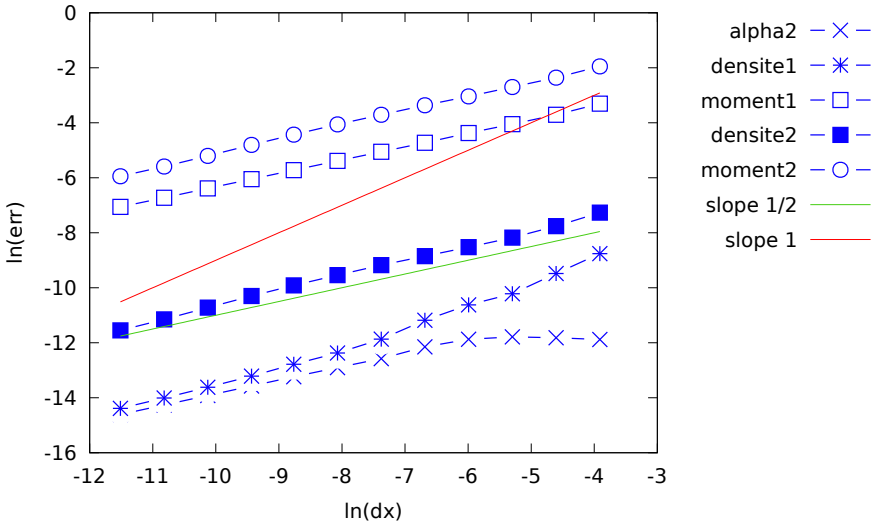

Figure 7: Stiffened gas EOS: Convergence curves for meshes containing from 100 to 100000 cells.

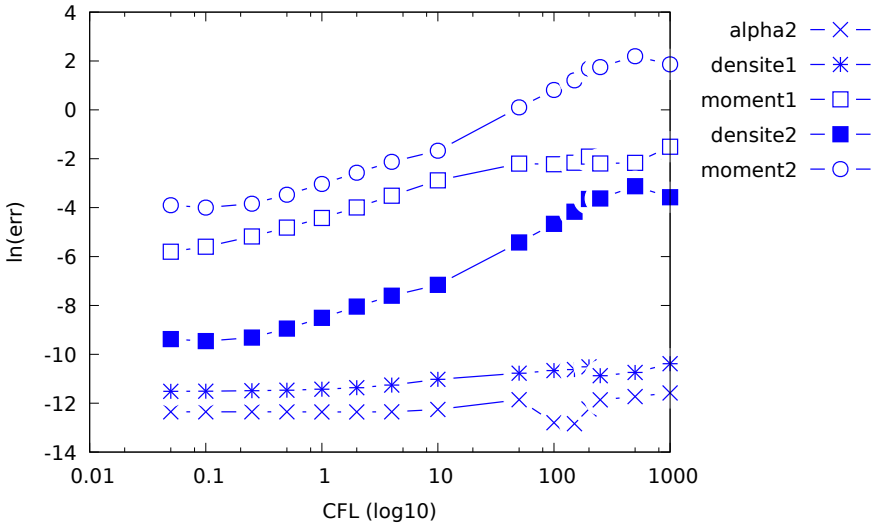

Figure 8: Stiffened gas EOS: Error with respect to the CFL_{u+c} number for a mesh containing 1000 cells. CFL_{u+c} number are between 0.05 and 1000.

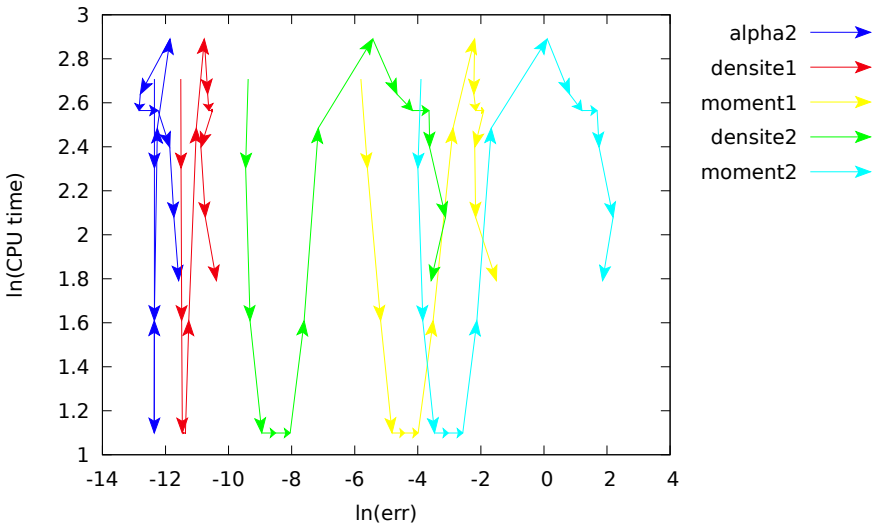

Figure 9: Stiffened gas EOS: CPU time with respect to the error for different CFL_{u+c} numbers for a mesh containing 1000 cells. CFL_{u+c} number belongs to $[0.05, 1000]$. The CFL_{u+c} number increases when following the arrows.

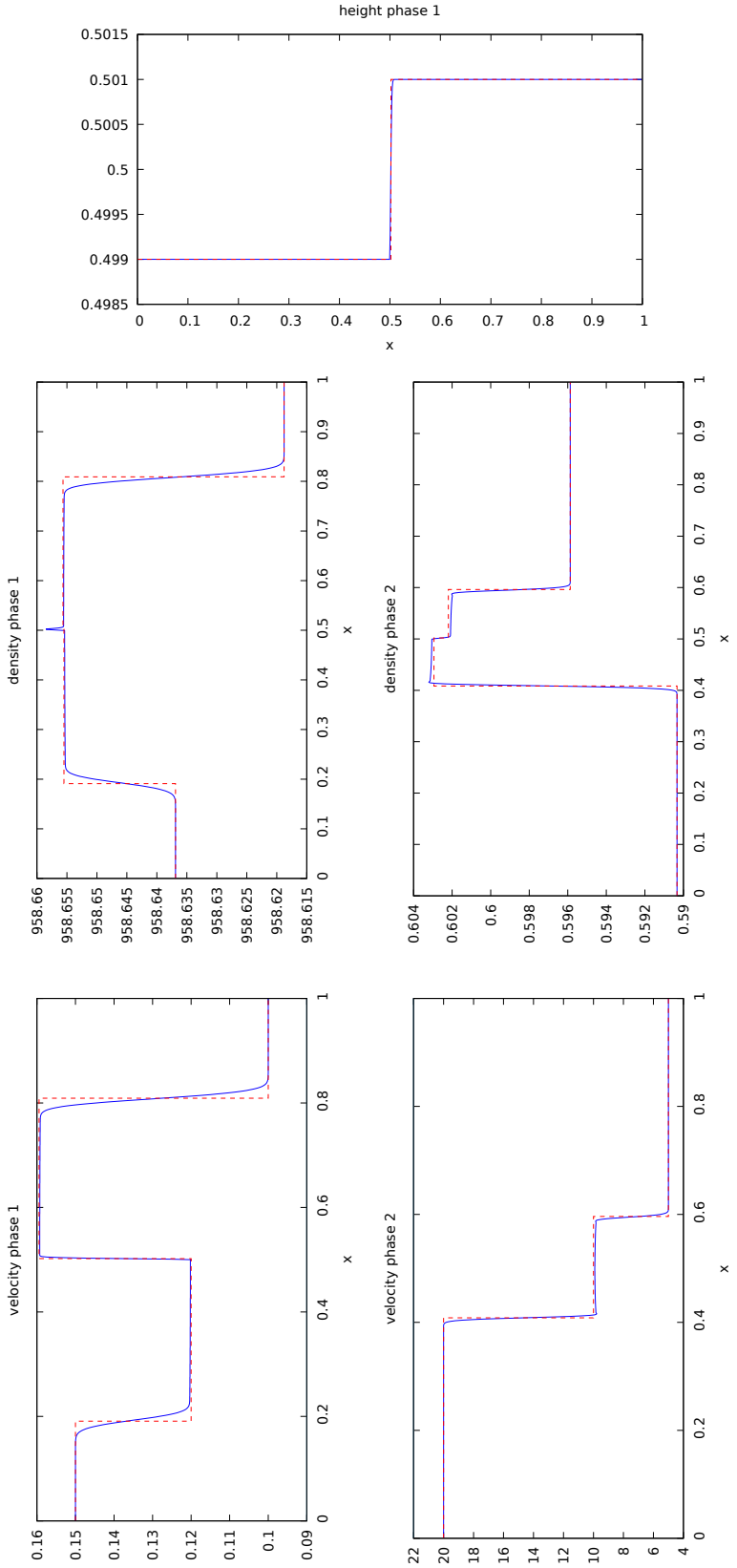

Figure 10: Stiffened gas EOS: Results for ρ_k and U_k for a mesh with 1000 cells and a CFL_{u+c} equal to 0.5 (blue lines), and the exact solution (red dashed line).

5 Effect of the relaxation source terms

In order to assess the behavior of the scheme when accounting for the relaxation source terms, we consider in this section a test case close to the conditions in the primary circuit of a nuclear power plant. The parameters of the EOS are now chosen to be representative of the conditions in the primary coolant circuit: $P = 1.5\ 10^7\ Pa$ and $T = 575.13\ K$. These parameters are here:

$$\gamma_1 = 1.01,\ \Pi_1 = 229578370.122306,\ E_1^0 = -3932082.63874524,\ K_1^0 = 380122.762540843,$$

for the liquid phase, and:

$$\gamma_2 = 1.4,\ \Pi_2 = -1781366.09450098,\ E_2^0 = 1131770.78371255,\ K_2^0 = 21954.1111467636.$$

for the gas phase.

	α_2	$\rho_1\ (kg/m^3)$	$U_1\ (m/s)$	$\rho_2\ (kg/m^3)$	$U_2\ (m/s)$
Y_L	0.1	606.513927223525	0	97.7109411153482	0
Y_R	0.2	603.513927223525	0	96.7109411153482	0

Table 3: Initial left and right states for the primary circuit test case.

The initial conditions consist in two uniform states separated by a discontinuity which is located at $x = 0.5$, the detailed values are given in table 3. With these conditions the pressure of both phases is close to $1.5\ 10^7\ Pa$. The height H of the pipe is equal to $0.1\ m$ and its length is $1\ m$. Computations are obtained for a mesh with 2000 cells and a CFL_{u+C} number equal to 0.5, which gives a time-step around $3.9\ 10^{-7}\ s$. We consider here the final time $T_{end} = 4\ 10^{-4}\ s$ and two sets of simulations are presented. The first one only accounts for velocity relaxation $\lambda_u = \{0, 10^5, 10^6, 10^9\}$ and without pressure relaxation $\lambda_{mp} = 0$. For the second set the pressure relaxation is examined by setting $\lambda_u = 10^6$ and $\lambda_{mp} = \{0, 10^3, 10^4, 10^6\}$. Since the densities have very different magnitudes, they have been normalized on the different plots by dividing them by the densities ρ_k of the left initial states (see in the third/fifth columns and first line of table 3).

Approximated solutions for the velocity-relaxation test cases are shown in figures 11 and 12. For the larger value of λ_u, the time scale of the velocity relaxation is smaller than the time-step so that for the current mesh we obtain an instantaneous velocity relaxation. The velocities tend to the mean velocity $U_m = (Q_1+Q_2)/(m_1+m_2)$ (thanks to the momentum conservation). Due to the high momentum of the liquid phase with respect to the gas-phase momentum for this test case, we have $U_m \sim U_1$. Thus the gas velocity decreases to $U_m \sim U_1$ when λ_u tends to $+\infty$. As a consequence, the fraction α_1 is convected with a lower velocity when λ_u increases. It should also be noted that for the larger value of λ_u high peaks appear on densities and pressures at the location of the strong variation of α_1.

Approximated solutions for the pressure-relaxation test cases are shown in figures 13 and 14. The larger value of λ_{mp} corresponds to an instantaneous pressure relaxation for the chosen mesh size and CFL_{u+C} number. For this test case, the velocity of the contact wave remains between $1.5\ m/s$ and $2\ m/s$. Hence, since the final time is small with respect to the time scale of the velocity, the location of the discontinuity of α_1 remains almost the same for all the values of λ_{mp}. The main modifications in the approximated solutions for α_1 due to pressure relaxation are the modification of the left/right values and the appearance of "intermediate states", see figures 14.

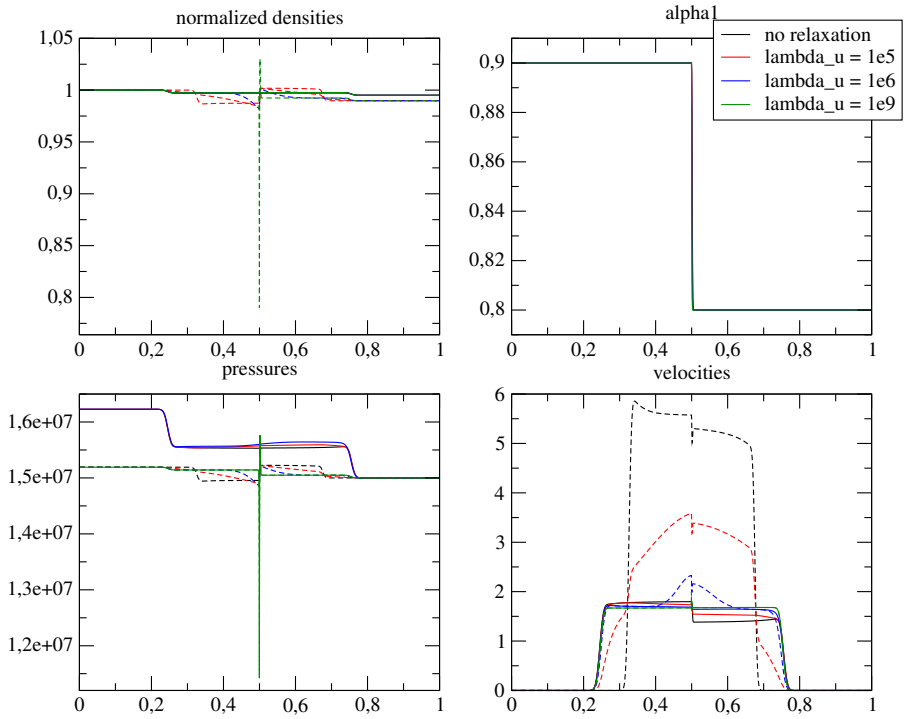

Figure 11: Approximated solutions for $\lambda_u = \{0, 10^5, 10^6, 10^9\}$ and $\lambda_{mp} = 0$. The plain (resp. dashed) lines represent the liquid (resp. gas) quantities.

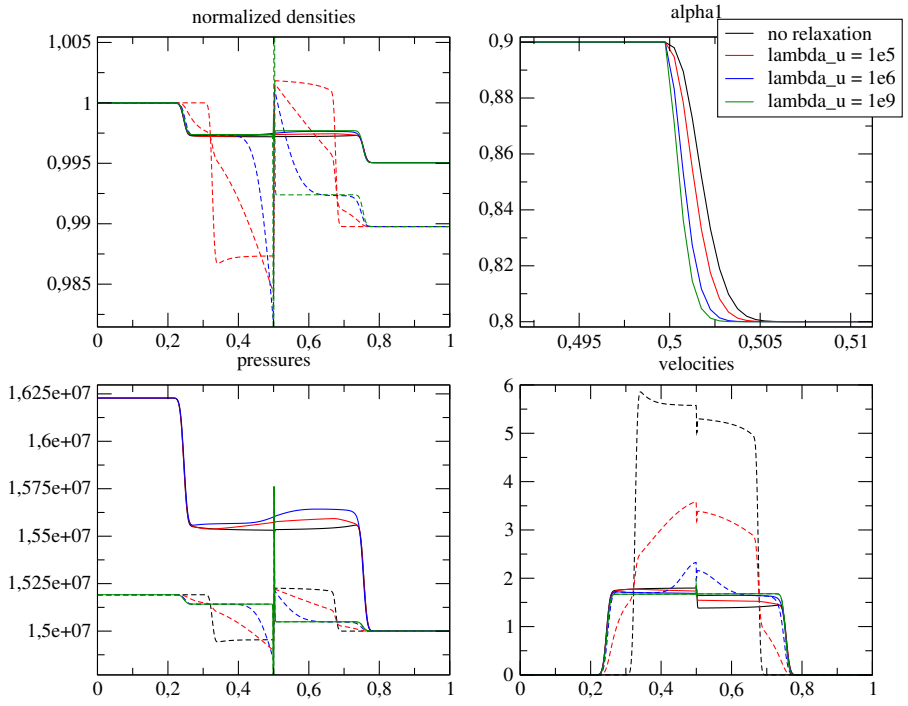

Figure 12: Zoom of the plots of figure 11.

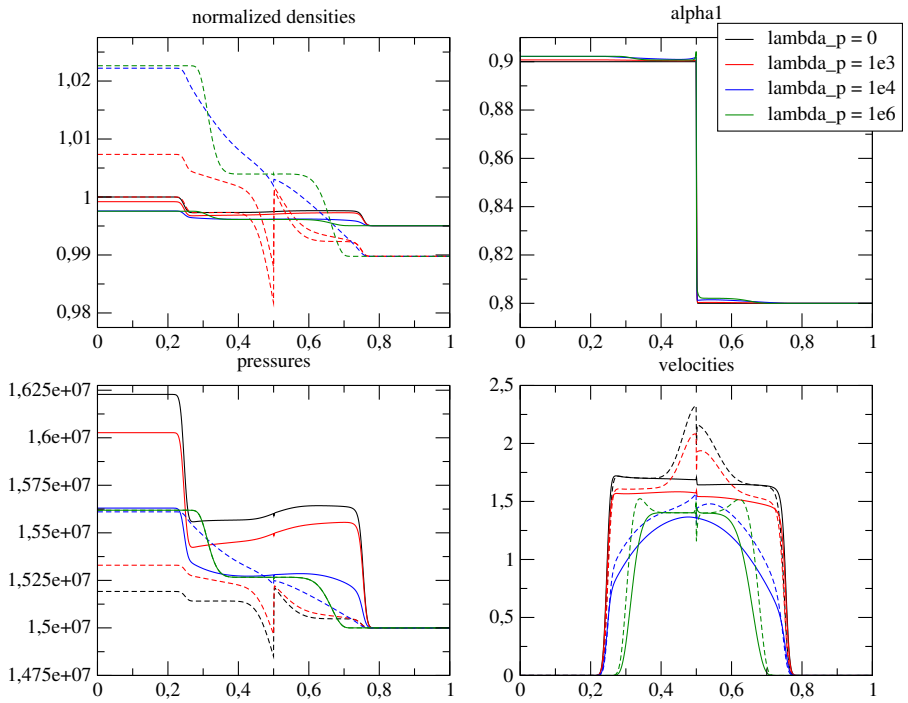

Figure 13: Approximated solutions for $\lambda_{mp} = \{0, 10^3, 10^4, 10^6\}$ and $\lambda_u = 10^6$. The plain (resp. dashed) lines represent the liquid (resp. gas) quantities.

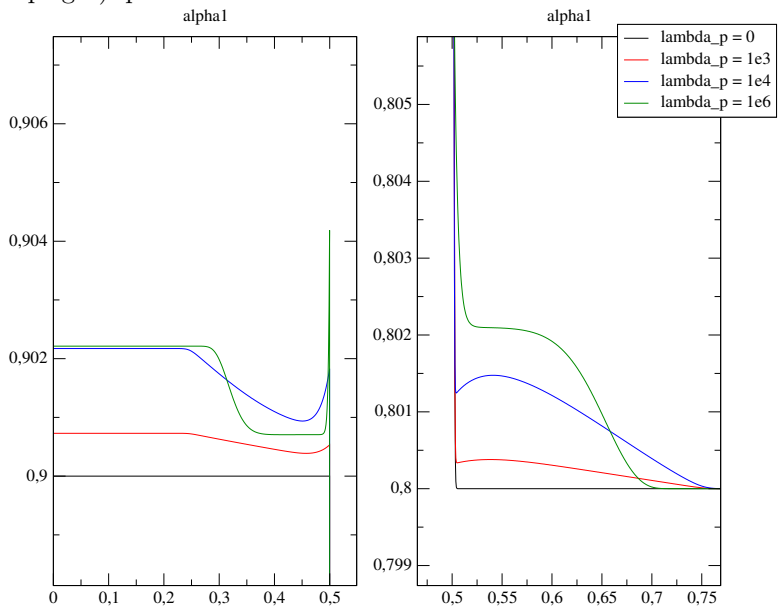

Figure 14: Zoom on the "intermediate states" created in the profile of the fraction α_1 by pressure relaxation.

6 Conclusion

In this work, classical techniques are used in order to build a scheme for the CTL model which is restricted to one-dimensional pipe flows [8, 9, 10]. Time discretization is performed through a SIMPLE-like splitting method, while discrete space-derivatives are computed on staggered meshes thanks to the MAC algorithm.

For compressible flows, the SIMPLE method remains stable even when using large time-steps with respect to the CFL_{u+c} limit. Nonetheless, even if the algorithm remains stable for large CFL_{u+c} numbers, the associated time-steps and mesh-sizes can become too large with respect to the physical scale of the density waves. As a consequence, in such situations the scheme provides less accurate approximated solutions of these density waves. The test cases of section 4 clearly show this behavior for Riemann problems involving density waves. Yet, it

should be noted that large time-steps allow to gain accuracy for the material waves. Hence, the time-step used to perform simulations should be chosen in agreement with the physical setting and with the targeted applications. If one is interested in computing the density waves, one should choose a time-step close to 1 with respect to CFL_{u+c}. On the contrary, if one only intends to get computational information about the advection of a scalar quantity for instance, a time-step close to 1 with respect to CFL_u can be preferred.

The CTL model is restricted to one-dimensional domains (pipe flows) [8, 9, 10]. The use of a MAC discretization technique is thus natural. Extending this approach to other two-phase flow models in two/three-dimensional domains - as the Baer-Nunziato model [1] for instance - could require other numerical schemes for the approximation of the spatial derivatives. If the computational domains of the targeted applications can be discretized using structured cartesian meshes, the present algorithm can be applied by using the 2D/3D extension of the MAC technique. On the contrary, if complex computational domains with unstructured meshes have to be treated, the space discretization technique should clearly be changed and one possible way could be to follow for instance the works [11, 12, 19, 18].

7 Appendix

7.1 Discretization of second order derivatives in space

We detail here the discretization of the second-order derivative operators on the primal mesh that arise in the second step of the algorithm. We thus consider here a term of the form $\partial_x \left(a(x)\partial_x \left(b(x)\right)\right)$ where a and b are primal quantities (i.e. they depend on α_k and/or m_k). Considering the cell i, we first approximate the derivative by a finite difference of two "fluxes" defined at the boundary of cell i:

$$\partial_x \left(a(x)\partial_x \left(b(x)\right)\right)_{|i} = \frac{\left(a(x)\partial_x \left(b(x)\right)\right)_{|i+1/2,i} - \left(a(x)\partial_x \left(b(x)\right)\right)_{|i-1/2,i}}{L_i} \tag{36}$$

Then, let us define the interface value $a_{i+1/2}$ such that:

$$\left(a(x)\partial_x \left(b(x)\right)\right)_{|i+1/2,i} = a_{i+1/2}\frac{b_{i+1} - b_i}{\widetilde{L}_i} \tag{37}$$

As we intend to build a conservative approximation, it is mandatory for the flux at the face $i+1/2$ to be equal when estimated in cell i and in its neighbooring cell $i+1$, that is:

$$\left(a(x)\partial_x \left(b(x)\right)\right)_{|i+1/2,i} = \left(a(x)\partial_x \left(b(x)\right)\right)_{|i+1/2,i+1}. \tag{38}$$

Since the fluxes in the relation above are respectively defined on cell i and $i+1$, we can define an interface value $b_{i+1/2}$ such that:

$$\left(a(x)\partial_x \left(b(x)\right)\right)_{|i+1/2,i} = a_i\frac{b_{i+1/2} - b_i}{\widetilde{L}_i/2}, \tag{39}$$

and

$$\left(a(x)\partial_x \left(b(x)\right)\right)_{|i+1/2,i+1} = a_{i+1}\frac{b_{i+1} - b_{i+1/2}}{\widetilde{L}_{i+1}/2}. \tag{40}$$

Then equation (38), (39) and (40) allow to explicitely express $b_{i+1/2}$ as:

$$b_{i+1/2} = \frac{b_i\ a_i/L_i + b_{i+1}\ a_{i+1}/L_{i+1}}{a_i/L_i + a_{i+1}/L_{i+1}}.$$

Moreover, the fluxes equality (38) should also hold for the formula (37):

$$a_{i+1/2}\frac{b_{i+1} - b_i}{\widetilde{L}_i} = \left(a(x)\partial_x \left(b(x)\right)\right)_{|i+1/2,i} = \left(a(x)\partial_x \left(b(x)\right)\right)_{|i+1/2,i+1} = a_{i+1}\frac{b_{i+1} - b_{i+1/2}}{\widetilde{L}_{i+1}/2}. \tag{41}$$

Hence we get from (41) and from the definition of $b_{i+1/2}$ an explicit formula for the interfacial term $a_{i+1/2}$:

$$a_{i+1/2} = (L_i + L_{i+1})\frac{a_i\ a_{i+1}}{a_{i+1}L_i + a_iL_{i+1}}.$$

Finally, considering that with the choices above for $a_{i+1/2}$ and $b_{i+1/2}$ the fluxes of relation (41) are equal, we define the flux at the face between cells i and $i+1$:

$$\left(a(x)\partial_x \left(b(x)\right)\right)_{|i+1/2} = a_{i+1/2}\frac{b_{i+1} - b_i}{\widetilde{L}_i} = \frac{2\ a_i\ a_{i+1}}{a_{i+1}L_i + a_iL_{i+1}}(b_{i+1} - b_i), \tag{42}$$

and the approximate of the second derivative term $\partial_x\left(a(x)\partial_x\left(b(x)\right)\right)$ is obtained from (36) and (42)

$$\partial_x\left(a(x)\partial_x\left(b(x)\right)\right)_{|i} = \frac{2\ a_i\ a_{i+1}}{a_{i+1}L_i + a_i L_{i+1}}\frac{(b_{i+1}-b_i)}{L_i} - \frac{2\ a_i\ a_{i-1}}{a_{i-1}L_i + a_i L_{i-1}}\frac{(b_i - b_{i-1})}{L_i}. \tag{43}$$

7.2 Convexity of the energies

We discuss in this section the convexity property of the different energies defined in section 2.2. For the two energies defined by (8) and (9), the proof is straightforward. Indeed, since the energies e_k are strictly convex we have $e_k'' > 0$, and we respectively get:

$$d^2_{\alpha_1\alpha_1}\mathcal{E}^{\#}_{0,\alpha} = \frac{e_1''(\alpha_1/m_1^0)}{m_1^0} + \frac{e_2''(\alpha_2/m_2^0)}{m_2^0} > 0,$$

and

$$d^2_{m_1m_1}\mathcal{E}^{\#}_{0,m} = \frac{e_1''(\alpha_1^0/m_1)}{m_1}\left(\frac{\alpha_1^0}{m_1}\right)^2 + \frac{e_2''(\alpha_2^0/(m^0-m_1))}{m^0-m_1}\left(\frac{\alpha_2^0}{m^0-m_1}\right)^2 > 0,$$

which leads to the conclusion that $\mathcal{E}^{\#}_{0,\alpha}$ and $\mathcal{E}^{\#}_{0,m}$ are strictly convex. From this derivatives, one also obtains that:

$$\partial^2_{\alpha_1\alpha_1}\left(\mathcal{E}_0^{\#}\right) = \frac{e_1''}{m_1} + \frac{e_2''}{m_2},$$

and

$$\partial^2_{m_1m_1}\left(\mathcal{E}_0^{\#}\right) = \frac{e_1''}{m_1}\left(\frac{\alpha_1}{m_1}\right)^2 + \frac{e_2''}{m_2}\left(\frac{\alpha_2}{m_2}\right)^2.$$

The cross derivative term for the energy $\mathcal{E}_0^{\#}$ reads:

$$\partial^2_{\alpha_1m_1}\left(\mathcal{E}_0^{\#}\right) = -\frac{e_1''}{m_1}\left(\frac{\alpha_1}{m_1}\right) - \frac{e_2''}{m_2}\left(\frac{\alpha_2}{m_2}\right) + \frac{gH}{2}.$$

We denote by $\nabla^2_{\alpha_1,m_1}\mathcal{E}_0^{\#}$ the Hessian matrix of $\mathcal{E}_0^{\#}$. According to the previous computations, we have:

$$\nabla^2_{\alpha_1,m_1}\mathcal{E}_0^{\#} = \frac{e_1''}{m_1}A_1 + \frac{e_2''}{m_2}A_2 + \frac{gH}{2}\begin{pmatrix} 0 & 1 \\ 1 & 0 \end{pmatrix},$$

where the matrices A_k:

$$A_k = \begin{pmatrix} 1 & -\frac{\alpha_k}{m_k} \\ -\frac{\alpha_k}{m_k} & \left(\frac{\alpha_k}{m_k}\right)^2 \end{pmatrix},$$

are symmetric definite positive (but not strictly definite positive since 0 is an eigenvalue). The characteristic polynomial associated with the Hessian reads:

$$\Pi(X) = X^2 - \left(\sum_k y_k(1+\tau_k^2)\right)\ X + \left(y_1y_2(\tau_1-\tau_2)^2 - gH\left(\frac{gH}{4} - \sum_k y_k\tau_k\right)\right),$$

where $y_k = e_k''/m_k > 0$ thanks to the strict convexity of e_k. Since $y_k > 0$ (and $\tau_k > 0$), a necessary and sufficient condition for the Hessian to be strictly definite positive is to have:

$$y_1y_2(\tau_1-\tau_2)^2 - gH\left(\frac{gH}{4} - \sum_k y_k\tau_k\right) > 0.$$

It must be recalled that the definition of the sound speed leads to the relation: $c_k^2 = \alpha_k y_k \tau_k$. A sufficient condition satisfying this condition is $gH/4 < \sum_k y_k\tau_k$ which can be written using the sound speeds:

$$\frac{gH}{4} = \left(\frac{1}{2}\sqrt{gH}\right)^2 < \frac{c_1^2}{\alpha_1} + \frac{c_2^2}{\alpha_2}$$

where $\sqrt{gH}$ can be seen as the speed of the gravity waves, and $\sqrt{gH}/2$ is defined as the group velocity of the gravity waves. Hence, if:

$$\frac{1}{2}\sqrt{gH} < \min(c_1, c_2), \tag{44}$$

then the energy $\mathcal{E}_0^{\#}$ is strictly convex with respect to (α_1, m_1).

The energy of system E has been defined in section 2.2 and it reads: $E = E_1 + E_1^p + E_2$. We then have:

$$E(\alpha_1, m_1, Q_1, \alpha_2, m_2, Q_2) = m_1 e_1\left(\frac{\alpha_1}{m_1}\right) + \alpha_1 m_1 \frac{gH}{2} + \frac{Q_1^2}{2m_1} + m_2 e_2\left(\frac{\alpha_2}{m_2}\right) + \frac{Q_2^2}{2m_2}. \tag{45}$$

It should be noted that we first consider the variable $(\alpha 1, m_1, Q_1, \alpha_2, m_2, Q_2)$ without imposing the constraint on the height fraction: $\alpha_1 + \alpha_2 = 1$. Hence, the energy E can be split into three contributions using a separation of variables:

$$E(\alpha 1, m_1, Q_1, \alpha_2, m_2, Q_2) = (E_1 + E_1^p)(\alpha_1, m_1, Q_1) + E_2(\alpha_2, m_2, Q_2).$$

Thanks to the previous results, we have:

$$\nabla^2_{\alpha_1, m_1, Q_1}(E_1 + E_1^p) = \frac{e_1''}{m_1}\begin{pmatrix} & A_1 & & 0 \\ & & & 0 \\ 0 & 0 & & 0 \end{pmatrix} + \frac{gH}{2}\begin{pmatrix} 0 & 1 & 0 \\ 1 & 0 & 0 \\ 0 & 0 & 0 \end{pmatrix} + \frac{1}{m_1}\begin{pmatrix} 0 & & 0 & 0 \\ 0 & & & \\ 0 & & B_1 & \end{pmatrix}, \tag{46}$$

and

$$\nabla^2_{\alpha_2, m_2, Q_2} E_2 = \frac{e_2''}{m_2}\begin{pmatrix} & A_2 & & 0 \\ & & & 0 \\ 0 & 0 & & 0 \end{pmatrix} + \frac{1}{m_2}\begin{pmatrix} 0 & & 0 & 0 \\ 0 & & & \\ 0 & & B_2 & \end{pmatrix}, \tag{47}$$

where the matrices B_k are symmetric definite positive:

$$B_k = \begin{pmatrix} \left(\frac{Q_k}{m_k}\right)^2 & -\frac{Q_k}{m_k} \\ -\frac{Q_k}{m_k} & 1 \end{pmatrix}.$$

Let us focus on the sum of the first two matrices of the Hessian (46) of the energy of phase 1. The characteristic polynomial of the latter is:

$$\Pi_1(X) = X^2 - y_1(1 + \tau_1^2)\, X + \left(y_1\tau_1(1 + y_1\tau_1) - \frac{gH}{2}\right).$$

A necessary and sufficient condition for the roots of the polynomial Π_1 to be positive is to have:

$$y_1\tau_1(1 + y_1\tau_1) \geq \frac{gH}{2}$$

Since $c_k^2 = \alpha_k y_k \tau_k$, the inequality above leads to:

$$\frac{gH}{2} \leq \frac{c_1^2}{\alpha_1}\left(\frac{c_1^2}{\alpha_1} + 1\right)$$

Hence if constraint (44) holds and if $c_1 > c_2 > 1$, we have:

$$\frac{gH}{2} \leq 2c_1^2 \leq 2\frac{c_1^2}{\alpha_1} < \frac{c_1^2}{\alpha_1}\left(\frac{c_1^2}{\alpha_1} + 1\right),$$

so that constraint (44) together with $c_1 > c_2 > 1$ is a sufficient condition for the roots of the polynomial Π_1 to be positive and thus for the sum of the first two matrices of the Hessian (46) to be symmetric definite positive. Since A_2, B_1 and B_2 are symmetric definite positive, we can conclude that the energy of the system E is convex with respect to $(\alpha 1, m_1, Q_1, \alpha_2, m_2, Q_2)$ when (44) holds. When adding the linear constraint $\alpha_1 + \alpha_2 = 1$ in the energy of the system, one can deduce that (44) and $c_1^2 > 1$ are also sufficient conditions for the energy E to be convex with respect to $(\alpha 1, m_1, Q_1, m_2, Q_2)$.

It should be recalled that subscript 1 denotes the liquid layer and subscript 2 denotes the gas layer. For two-layer flows described by the CTL model, the constraint $c_1 > c_2 > 1$ is thus generally fulfilled in a very large range of industrial situations.

References

[1] M.R. Baer and J.W. Nunziato. A two-phase mixture theory for the Deflagration-To-Detonation transition (DDT) in reactive granular materials. *Journal of Multiphase Flows*, 12:861–889, 1986.

[2] V Casulli and D Greenspan. Pressure method for the numerical solution of transient, compressible fluid flows. *International Journal for Numerical Methods in Fluids*, 4(11):1001–1012, 1984.

[3] Alexandre Chiapolino and Richard Saurel. Models and methods for two-layer shallow water flows. *Journal of Computational Physics*, 371:1043–1066, 2018.

[4] Alexandre Joel Chorin. Numerical solution of the navier-stokes equations. *Mathematics of computation*, 22(104):745–762, 1968.

[5] Phillip Colella and Karen Pao. A projection method for low speed flows. *Journal of Computational Physics*, 149(2):245–269, 1999.

[6] Frédéric Coquel, Khaled Saleh, and Nicolas Seguin. A robust and entropy-satisfying numerical scheme for fluid flows in discontinuous nozzles. *Mathematical Models and Methods in Applied Sciences*, 24(10):2043–2083, 2014.

[7] Sophie Dallet. A comparative study of numerical schemes for the baer-nunziato model. *International Journal on Finite Volumes*, 13:1–37, 2016.

[8] Charles Demay. *Modélisation et simulation d'écoulements transitoires diphasiques eau-air dans les circuits hydrauliques*. Theses, Université Grenoble Alpes, November 2017.

[9] Charles Demay, Christian Bourdarias, Benoît de Laage de Meux, Stéphane Gerbi, and Jean-Marc Hérard. A splitting method adapted to the simulation of mixed flows in pipes with a compressible two-layer model. *ESAIM: Mathematical Modelling and Numerical Analysis*, 53(2):405–442, 2019.

[10] Charles Demay and Jean-Marc Hérard. A compressible two-layer model for transient gas–liquid flows in pipes. *Continuum Mechanics and Thermodynamics*, 29(2):385–410, 2017.

[11] Robert Eymard and Raphaèle Herbin. A staggered finite volume scheme on general meshes for the Navier-Stokes equations in two space dimensions. *International Journal on Finite Volumes*, 2(1):1–18, 2005.

[12] Laura Gastaldo, Raphaele Herbin, Walid Kheriji, Céline Lapuerta, and J-C Latché. Staggered discretizations, pressure correction schemes and all speed barotropic flows. In *Finite Volumes for Complex Applications VI Problems & Perspectives*, pages 839–855. Springer, 2011.

[13] Francis H Harlow and Anthony A Amsden. Numerical calculation of almost incompressible flow. *Journal of Computational Physics*, 3(1):80–93, 1968.

[14] Francis H Harlow and Anthony A Amsden. A numerical fluid dynamics calculation method for all flow speeds. *Journal of Computational Physics*, 8(2):197–213, 1971.

[15] Francis H Harlow and J Eddie Welch. Numerical calculation of time-dependent viscous incompressible flow of fluid with free surface. *Physics of fluids*, 8(12):2182–2189, 1965.

[16] Jean-Marc Hérard and Olivier Hurisse. Computing two-fluid models of compressible water-vapour flows with mass transfer. In *42nd AIAA Fluid Dynamics Conference and Exhibit*, page 2959, 2012.

[17] Jean-Marc Hérard and Olivier Hurisse. A fractional step method to compute a class of compressible gas–liquid flows. *Computers & Fluids*, 55:57–69, 2012.

[18] Raphaele Herbin, Walid Kheriji, and J-C Latché. On some implicit and semi-implicit staggered schemes for the shallow water and euler equations. *ESAIM: Mathematical Modelling and Numerical Analysis*, 48(6):1807–1857, 2014.

[19] Raphaèle Herbin, J-C Latché, and Trung Tan Nguyen. Explicit staggered schemes for the compressible euler equations. In *ESAIM: Proceedings*, volume 40, pages 83–102. EDP Sciences, 2013.

[20] O. Hurisse. Various choices of source terms for a class of two-fluid two-velocity models. *ESAIM: Mathematical Modelling and Numerical Analysis*, 55(2):357–380, 2021.

[21] Raad I Issa. Solution of the implicitly discretised fluid flow equations by operator-splitting. *Journal of computational physics*, 62(1):40–65, 1986.

[22] KC Karki and SV Patankar. Pressure based calculation procedure for viscous flows at all speeds in arbitrary configurations. *AIAA journal*, 27(9):1167–1174, 1989.

[23] Yujie Liu. *Contribution to the verification and the validation of an unsteady two-phase flow model.* Theses, Aix-Marseille Université, September 2013.

[24] Hippolyte Lochon. *Modélisation et simulation d'écoulements transitoires eau-vapeur en approche bifluide.* Theses, Aix Marseille Université, October 2016.

[25] Marica Pelanti and Keh-Ming Shyue. A numerical model for multiphase liquid–vapor–gas flows with interfaces and cavitation. *International Journal of Multiphase Flow*, 113:208–230, 2019.

[26] Khaled Saleh and Nicolas Seguin. Some mathematical properties of a barotropic multiphase flow model. *ESAIM: Proceedings and Surveys*, 69:70–78, 2020.

[27] Richard Saurel and Olivier Lemetayer. A multiphase model for compressible flows with interfaces, shocks, detonation waves and cavitation. *Journal of Fluid Mechanics*, 431:239, 2001.

[28] Richard Saurel and Carlos Pantano. Diffuse-interface capturing methods for compressible two-phase flows. *Annual Review of Fluid Mechanics*, 50:105–130, 2018.